Available online at www.sciencedirect.com
SCIENCE DIRECT®
Journal of Computational Physics 205 (2005) 108–130
JOURNAL OF COMPUTATIONAL PHYSICS
www.elsevier.com/locate/jcp

A second order kinetic scheme for gas dynamics on arbitrary grids

Benjamin Keen [a,b,*,1], Smadar Karni [a,2]

[a] Department of Mathematics, University of Michigan, 525 E. University Avenue, Room 2074, Ann Arbor, MI 48109-1109, USA
[b] IDA Center for Computing Sciences, 17100 Science Drive Bowie, MD 20715, USA

Received 24 November 2003; received in revised form 20 September 2004; accepted 2 November 2004

Abstract

Cartesian meshes for domains with complicated boundaries give rise to cut cells with arbitrarily small volumes. Explicit integration schemes over such meshes have a time step restriction proportional to the smallest cell volume. We present an implementation of the kinetic scheme for gas dynamics by Perthame [B. Perthame, Boltzmann type schemes for gas dynamics and the entropy property. SIAM J. Num. Anal. 27 (1990) 1405–1421] on arbitrary Cartesian meshes. The formulation allows a time step based on the underlying regular cell size, and retains L_1-stability, positivity and second order convergence. Numerical convergence studies on arbitrary grids are presented.
© 2004 Published by Elsevier Inc.

MSC: 65M12; MSC 76P05; MSC 76N15
Keywords: Compressible flow; Cartesian meshes; Numerical methods; Kinetic schemes; Small cell stability

1. Introduction

Computations of practical engineering problems often involve domains with complicated boundaries. Examples include external flow around aircraft, or internal flow inside engines. Grid generation around such geometries forms an important component in a successful computation, presenting practical challenges in the scientific computing process. Body-fitted coordinates are often very difficult to generate, while

* Corresponding author. Tel.: +301 805 7501.
E-mail addresses: bjkeen@super.org (B. Keen), karni@umich.edu (S. Karni).
[1] Supported by the Krell Institute Computational Science Graduate Fellowship of the Department of Energy, Grant Number DE-FG02-97ER25308.
[2] Supported in part by NSF Grant # DMS-9973291.

0021-9991/$ - see front matter © 2004 Published by Elsevier Inc.
doi:10.1016/j.jcp.2004.11.002

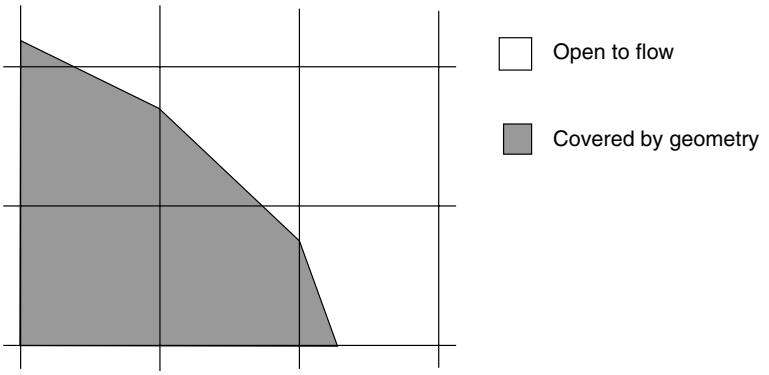

Fig. 1. A Cartesian mesh grid has regular, irregular and covered cells.

unstructured triangular meshes do not lend themselves easily to to adaptive mesh refinement. Cartesian grids are relatively easy to generate in any number of space dimensions, and lend themselves to grid adaption [1]. However, such grids lose their regular structure near domain boundaries where cut cells of odd shapes and arbitrary size may arise (See Fig. 1.) Explicit, time accurate schemes for integrating the gas dynamics equations have a CFL time step restriction proportional to the size of the smallest cell. Since irregular cut cells may be arbitrarily small, such a restriction is impractical and is often referred to as the 'small cell problem'. Scheme modifications to overcome the small cell problem include cell merging, and flux redistribution. In cell merging [2], the small cell is merged with a nearby regular cell, thereby ensuring a lower bound on cell size and alleviating the time step restriction. Flux redistribution schemes [3,4] first create a preliminary solution update ignoring the presence of the boundary, then hybridize it with the solution update of the small cell to form a stable update. The conservation error is distributed among the small cell's neighbors, keeping the scheme as a whole conservative. The use of capacity functions in the case of advection [5] and long time step methods [6] also can serve to stabilize small cells. A more recent approach is the h-box method, which devises a numerical flux for the small cells using a domain of dependence of regular grid spacing h; see [7] and papers it cites. With all such techniques there is the concern that the boundary treatment remains as accurate as the interior scheme: see [8].

In this paper, we formulate the kinetic scheme for gas dynamics proposed by Perthame in [9] on arbitrary grids. The formulation overcomes the small cell problem by accounting for particles transported through more than one cell face. The scheme retains its regular grid robustness, is L_1-stable and positive, and requires no additional averaging near the domain boundaries. A similar approach to this problem, computing conservative transport directly between grid cells, is taken in [10].

The paper is organized as follows: Section 2 introduces the governing equations and notation, and discusses the general numerical framework along with the basic scheme properties. Section 3 describes an implementation of the scheme on arbitrary grid, and Section 4 presents extensive numerical examples for one dimensional flows. Section 5 sketches the 2D form of the scheme, and Section 6 gives numerical examples for 2D flows.

2. Preliminaries

2.1. Macroscopic gas dynamics

The Euler equations of gas dynamics in one space dimension are

$$\begin{pmatrix} \rho \\ \rho u \\ E \end{pmatrix}_t + \begin{pmatrix} \rho u \\ \rho u^2 + p \\ u(E+p) \end{pmatrix}_x = 0, \tag{1}$$

where ρ, u and p denote the density, bulk velocity, and pressure. The total energy is $E = \rho e + \frac{1}{2}\rho u^2$, with e the specific internal energy. The system is closed by an equation of state; for polytropic gases it is

$$p = (\gamma - 1)\rho e, \tag{2}$$

for γ the specific heat ratio of the gas. The equations (1) form a set of non-linear hyperbolic conservation laws

$$\mathbf{U}_t + \mathbf{F}(\mathbf{U})_x = 0 \tag{3}$$

with $\mathbf{U} = (\rho, \rho u, E)^{\mathrm{T}}$ the vector of conserved variables and $\mathbf{F}(\mathbf{U}) = (\rho u, \rho u^2 + p, u(E + p))^{\mathrm{T}}$ the vector of flux functions.

2.2. Finite volume numerical approximation

We partition the computational domain into cells $\mathscr{I}_i = [x_{i-\frac{1}{2}}, x_{i+\frac{1}{2}}]$, of length Δx_i and define a set of discrete times $\{t^n\}$. Integrating (3) over the box $\mathscr{I}_i \times [t^n, t^{n+1}]$ gives

$$\mathbf{U}_i^{n+1} = \mathbf{U}_i^n - \frac{\Delta t}{\Delta x_i}\left(\mathbf{F}_{i+\frac{1}{2}}^n - \mathbf{F}_{i-\frac{1}{2}}^n\right), \tag{4}$$

where

$$\mathbf{U}_i^n = \frac{1}{\Delta x_i}\int_{\mathscr{I}_i} \mathbf{U}(x, t^n)\,\mathrm{d}x, \quad \mathbf{F}_{i+\frac{1}{2}}^n = \frac{1}{\Delta t}\int_{t^n}^{t^{n+1}} \mathbf{F}(\mathbf{U}(x_{i+\frac{1}{2}}, t))\,\mathrm{d}t \tag{5}$$

are, respectively, the cell average of $\mathbf{U}$ over $\mathscr{I}_i$ at time t^n, and the time average of $\mathbf{F}(\mathbf{U})$ at $x_{i+\frac{1}{2}}$ over the time interval $[t^n, t^{n+1}]$. Finite volume schemes are obtained by approximating the time-average flux $\mathbf{F}_{i+\frac{1}{2}}^n$ at cell interfaces. In kinetic schemes, the Boltzmann equation (6) is used to determine the flux, as described below. We have adopted the kinetic scheme derived by Perthame [9] for computations on arbitrary grids; for completeness it is described in Section 2.3.

2.3. The kinetic framework

The evolution of non-equilibrium gas dynamics is governed by the Boltzmann equation:

$$f_t + \mathbf{v}\cdot\nabla_{\mathbf{x}} f = Q(f, f). \tag{6}$$

The function $f(t, x; v)$ is the particle distribution function in v, the particle velocity. The collision operator $Q(f, f)$ governs relaxation processes toward thermal equilibrium, for which f takes the form of a Maxwellian distribution. Macroscopic descriptions of gas dynamics such as (1) may be obtained by taking moments in v of (6) and the appropriate fluid limit [11].

For its equilibrium distribution, the kinetic scheme proposed by Perthame [9] uses a simplified pseudo-Maxwellian that retains some properties of the Maxwellian with respect to its moments. Define

$$\chi(w) = (2\sqrt{3})^{-1}\mathbb{I}_{[-\sqrt{3},\sqrt{3}]}(w), \tag{7}$$

where $\mathbb{I}_{\mathscr{S}}(x)$ is the characteristic function of $\mathscr{S}$. The moments

$$m_k = \int_{\mathbb{R}} w^k \chi(w)\,\mathrm{d}w \tag{8}$$

satisfy

$$m_0 = m_2 = 1; \quad m_{2i+1} = 0, \ i \geqslant 0.$$

The particle 'equilibrium' distribution is defined in terms of $f(v)$ and $g(v)$:

$$f(v) = \frac{\rho}{\sqrt{T}}\chi(w(v)); \quad g(v) = \lambda\sqrt{T}\chi(w(v)), \tag{9}$$

where $T = p/\rho$ is the temperature, $\lambda = (\gamma - 1)^{-1} - 1/2$, and

$$w = \frac{v - u}{\sqrt{T}} \tag{10}$$

is a rescaled, non-dimensional particle velocity relative to the gas macroscopic velocity u. The pseudo-Maxwellian (7) has compact support which implies a maximum particle speed, so for a given time step the domain of influence of each grid cell is known. A direct calculation confirms that

$$\int_{\mathbb{R}} \begin{pmatrix} 1 \\ v \\ \frac{v^2}{2} \end{pmatrix} f(v) + \begin{pmatrix} 0 \\ 0 \\ 1 \end{pmatrix} g(v)\,\mathrm{d}v = \begin{pmatrix} \rho \\ \rho u \\ E \end{pmatrix} \equiv \mathbf{U} \tag{11}$$

and

$$\int_{\mathbb{R}} \begin{pmatrix} 1 \\ v \\ \frac{v^2}{2} \end{pmatrix} v\, f(v) + \begin{pmatrix} 0 \\ 0 \\ 1 \end{pmatrix} v\, g(v)\,\mathrm{d}v = \begin{pmatrix} \rho u \\ \rho u^2 + p \\ u(E + p) \end{pmatrix} \equiv \mathbf{F}(\mathbf{U}). \tag{12}$$

Within the kinetic framework, given piecewise constant initial data $\mathbf{U}_i^n$, the 'pseudo-equilibrium' particle distributions $f_0(x; v)$ and $g_0(x; v)$ are constructed in each cell, according to (9). The idea is to solve the collisionless transport equations:

$$\begin{aligned} &f_t + v \cdot \nabla_x f = 0, \quad f(x, 0; v) = f_0(x; v), \\ &g_t + v \cdot \nabla_x g = 0, \quad g(x, 0; v) = g_0(x; v). \end{aligned} \tag{13}$$

These are linear transport equations and can be solved exactly:

$$\begin{aligned} &f(x, \Delta t; v) = f_0(x - v\Delta t; v), \\ &g(x, \Delta t; v) = g_0(x - v\Delta t; v). \end{aligned} \tag{14}$$

Macroscopic fluid data at the new time level is recovered by taking moments in v of the distribution functions using (11) and averaging over each cell. Once the fluid variables at $t = \Delta t$ have been obtained, instantaneous relaxation to thermal equilibrium is assumed by reconstructing the particle distribution function as an 'equilibrium' distribution around the newly computed macroscopic state.

2.4. Scheme properties

The time marching scheme (9), (13), (14) is inherently conservative. It is L_1-stable and entropy satisfying provided f_0 and g_0 are non-negative [12]; it is time accurate to first order, pointwise (and thus for cell averages), and it preserves positivity of density and internal energy. More details can be found in [9].

Second order time accuracy may be obtained by modifying the initial distributions $f(x; v)$ and $g(x; v)$ to take the form

$$f_s(x; v) = f_0(x; v)\big(1 - a(x)(w^2 - 1)\big), \tag{15}$$

$$g_s(x;v) = g_0(x;v)\left(1 - \frac{2}{5\lambda}a(x) + \lambda^{-1}b(x)w\right). \tag{16}$$

A direct calculation establishes that with the choice

$$a(x) = \frac{5\Delta t}{8}(3-\gamma)\partial_x u_0(x), \tag{17}$$

$$b(x) = \Delta t\left[\left(-6/5 - \frac{\gamma}{\gamma-1}\right)\partial_x\sqrt{T_0(x)} - \frac{3}{10}\sqrt{T_0(x)}\frac{\partial_x\rho_0(x)}{\rho_0(x)}\right], \tag{18}$$

$\mathbf{U}$ may be recovered from f_s and g_s just as in (11), and that the Taylor expansion in time of the kinetic solution matches that of the exact solution including terms of $O(\Delta t^2)$. To ensure positivity of f_s and g_s, a and b need to be limited. For gas dynamics, $1 < \gamma \leqslant 5/3$, resulting in the restriction

$$|a| \leqslant 1/2, \quad |b| \leqslant (\lambda - 1/5)/\sqrt{3}. \tag{19}$$

Second order spatial accuracy is obtained through a piecewise linear reconstruction using the primitive variables $V = (\rho, u, r \equiv \sqrt{T})$

$$\mathbf{V}_i(x) = (\rho_i(x), u_i(x), r_i(x))^{\mathrm{T}} = (\rho_i, u_i, r_i) + (\mathsf{D}\rho_i, \mathsf{D}u_i, \mathsf{D}r_i)(x - x_i). \tag{20}$$

To ensure the reconstruction is conservative, we set

$$\rho_i = \rho_i^n, \tag{21}$$

$$u_i = \left((\rho u)_i^n - \frac{\mathsf{D}\rho_i \mathsf{D}u_i}{12}\Delta x_i^2\right)/\rho_i^n \tag{22}$$

and r_i the positive root of

$$\frac{\rho_i^n}{\gamma-1}r^2 + \frac{\Delta x_i^2}{6}\frac{\mathsf{D}\rho_i \mathsf{D}r_i}{(\gamma-1)}r + \frac{\rho_i^n}{2}\frac{u_i^2}{2} + \frac{\Delta x_i^2}{12}\left(\frac{\rho_i^n \mathsf{D}r_i^2}{(\gamma-1)} + \frac{\rho_i^n \mathsf{D}u_i^2}{2} + u_i \mathsf{D}u_i \mathsf{D}\rho_i\right) = E_i^n. \tag{23}$$

To ensure positivity of $r_i(x)$ we limit

$$|\mathsf{D}u_i| \leqslant \frac{2\sqrt{(\gamma-1)T_i}}{\Delta x_i}, \tag{24}$$

$$|\mathsf{D}r_i| \leqslant \frac{\sqrt{T_i}}{\sqrt{3}\Delta x_i}, \tag{25}$$

where T_i is calculated from the cell averaged state $\mathbf{U}_i^n$.

3. Numerical implementation

In [9], the scheme is given in finite volume form with $\mathbf{F}_{i+\frac{1}{2}} = \mathbf{F}^+_{i+\frac{1}{2}} + \mathbf{F}^-_{i+\frac{1}{2}}$, where

$$\mathbf{F}^+_{i+\frac{1}{2}} = \frac{1}{\Delta t}\int_0^{\Delta t}\int_{v>0}\begin{pmatrix} v \\ v^2 \\ \frac{v^3}{2}\end{pmatrix} f_i(x_{i+\frac{1}{2}}, t; v) + \begin{pmatrix} 0 \\ 0 \\ v\end{pmatrix} g_i(x_{i+\frac{1}{2}}, t; v)\,\mathrm{d}v\,\mathrm{d}t, \tag{26}$$

$$\mathbf{F}^{-}_{i+\frac{1}{2}} = \frac{1}{\Delta t}\int_0^{\Delta t}\int_{v<0}\begin{pmatrix} v \\ v^2 \\ \frac{v^3}{2}\end{pmatrix} f_{i+1}(x_{i+\frac{1}{2}}, t; v) + \begin{pmatrix} 0 \\ 0 \\ v\end{pmatrix} g_{i+1}(x_{i+\frac{1}{2}}, t; v)\,\mathrm{d}v\,\mathrm{d}t. \tag{27}$$

Here

$$f_i(x; v) = f_s(x; v)\mathbb{I}_{\mathscr{I}_i}(x), \quad g_i(x; v) = g_s(x; v)\mathbb{I}_{\mathscr{I}_i}(x) \tag{28}$$

are the distributions in cell $\mathscr{I}_i$. The flux at $x_{i+\frac{1}{2}}$ is composed of contributions from its neighbors to the immediate left and right; see Fig. 2. If particles are allowed to cross at most one cell interface during a time step, the CFL restriction for (13), based on the maximum particle speed in (7), limits the timestep to

$$\Delta t \leqslant \frac{\min_i \Delta x_i}{\max_i(|u_i| + \sqrt{3T_i})}. \tag{29}$$

In the case of embedded boundaries, the smallest cell size $\min_i \Delta x_i$ may be arbitrarily small, leading to a prohibitively small time step Δt. A larger time step may be taken, during which particles may travel across multiple cell faces. The flux formulation (26) is not easy to generalize for particles that travel across multiple faces in a single time step. Instead, we calculate the transport of particles directly between nearby cells that do not necessarily share a common face. We set the desired domain of dependence of the transport independently of the smallest cell size of the grid; see Fig. 3.

We will set Δt similarly to (29):

$$\Delta t \leqslant \frac{\Delta x}{\max_i\{|u_i| + \sqrt{3T_i}\}}. \tag{30}$$

The difference is that the parameter Δx is chosen independent of the smallest cell size. For cut-cell grids, the regular grid spacing Δx is used.

3.1. Basic transport problem

The conserved quantities in cell $\mathscr{I}_i$ at time Δt,

$$\mathbf{U}_i(\Delta t) = \int_{x\in\mathscr{I}_i}\int_{v\in\mathbb{R}}\begin{pmatrix} 1 \\ v \\ \frac{v^2}{2}\end{pmatrix} f(x, v, \Delta t) + \begin{pmatrix} 0 \\ 0 \\ 1\end{pmatrix} g(x, v, \Delta t)\,\mathrm{d}v\,\mathrm{d}x \tag{31}$$

can be calculated using the exact solution to the transport equation (13):

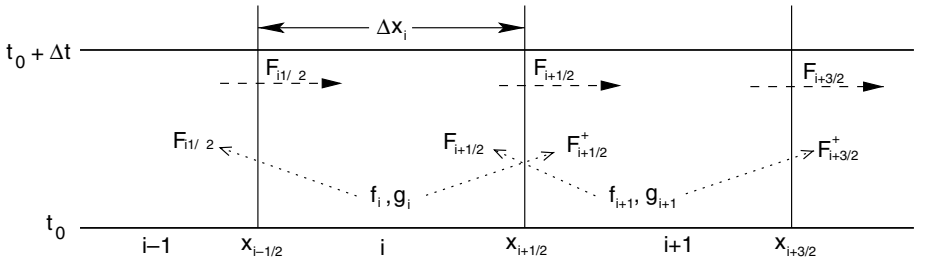

Fig. 2. Flux formulation.

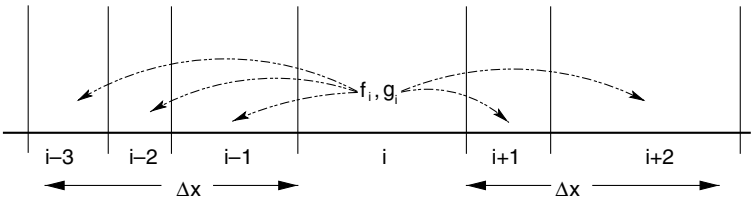

Fig. 3. Direct transport formulation.

$$\mathbf{U}_i(\Delta t) = \sum_j \int_{x\in\mathscr{I}_i}\int_{v\in\mathbb{R}} \begin{pmatrix} 1 \\ v \\ \frac{v^2}{2} \end{pmatrix} f_j(x - v\Delta t, v) + \begin{pmatrix} 0 \\ 0 \\ 1 \end{pmatrix} g_j(x - v\Delta t, v)\,\mathrm{d}v\,\mathrm{d}x. \tag{32}$$

The size of Δx and the corresponding choice of Δt set the domain of dependence of the transport, so we sum over those cells $\mathscr{I}_j$ within Δx of $\mathscr{I}_i$.

It is sufficient to describe the transport of particles that originate in a (source) grid cell $\mathscr{S} = \mathscr{I}_j = [-\frac{\Delta x_j}{2}, \frac{\Delta x_j}{2}]$ and end in another (target) grid cell $\mathscr{T} = \mathscr{I}_i$ at time Δt:

$$\int_{x\in\mathscr{S}}\int_{x+v\Delta t\in\mathscr{T}} \begin{pmatrix} 1 \\ v \\ \frac{v^2}{2} \end{pmatrix} f_j(x, v) + \begin{pmatrix} 0 \\ 0 \\ 1 \end{pmatrix} g_j(x, v)\,\mathrm{d}v\,\mathrm{d}x. \tag{33}$$

The support in v of f_j and g_j is determined by $\chi(w)$. Recalling the definition of $\chi(w)$ (7) and w (10) we set

$$\chi(w(v)) = (2\sqrt{3})^{-1}\mathbb{I}_{[q_-(x),q_+(x)]}(v), \tag{34}$$

where

$$q_\pm(x) = u_j \pm \sqrt{3}r_j + (\mathsf{D}u_j \pm \sqrt{3}\mathsf{D}r_j)x, \tag{35}$$

are the maximal and minimal particle velocities in the source cell j.

Then, using (15), (16) and (34) we may rewrite (33) as

$$(2\sqrt{3})^{-1}\int_{x\in\mathscr{S}}\int_{\substack{x+v\Delta t\in\mathscr{T} \\ v\in[q_-(x),\ q_+(x)]}} \begin{pmatrix} 1 \\ v \\ \frac{v^2}{2} \end{pmatrix} \mathrm{I} + \begin{pmatrix} 0 \\ 0 \\ 1 \end{pmatrix} \mathrm{II}\,\mathrm{d}v\,\mathrm{d}x. \tag{36}$$

where

$$\mathrm{I} = \frac{\rho_j + \mathsf{D}\rho_j x}{r_j + \mathsf{D}r_j x}\Big(1 + a_j(w(x,v)^2 - 1)\Big) \tag{37}$$

$$\mathrm{II} = (\rho_j + \mathsf{D}\rho_j x)(r_j + \mathsf{D}r_j x)\left(\lambda - \frac{2a_j}{5} + b_j(x)w(x,v)\right) \tag{38}$$

are the contributions due to $f_j(x; v)$ and $g_j(x; v)$, respectively.

3.2. The integral

For second order accuracy, we approximate the integrand of (36) by a Taylor expansion in x, dropping terms of order $\mathrm{O}(x^2)$ and higher. Then,

$$\mathrm{I} = \frac{\rho}{r}\left((1 + \frac{\mathsf{D}\rho}{\rho}x - \frac{\mathsf{D}r}{r}x) + a\Big((v-u)^2 r^{-2} - 1\Big)\right) + \mathrm{O}(\Delta x^2), \tag{39}$$

and

$$\mathrm{II} = A(\rho r + \rho \mathsf{D}r x + r\mathsf{D}\rho x) + (\rho B_1 + rB_2)(v-u) + \mathrm{O}(\Delta x^2), \tag{40}$$

where

$$\begin{aligned} A &= \lambda - 2a/5, \\ B_1 &= \Delta t\left(-6/5 + \frac{\gamma}{\gamma - 1}\right)\mathsf{D}r, \\ B_2 &= -\frac{3}{10}\Delta t \mathsf{D}\rho. \end{aligned} \tag{41}$$

To compute (36) we need to evaluate integrals of the form

$$\int_{x\in\mathscr{S}} \int_{\substack{x+v\Delta t\in\mathscr{T} \\ v\in[q_-,q_+]}} x^i v^j \,\mathrm{d}v\,\mathrm{d}x. \tag{42}$$

for $0 \leqslant j \leqslant 4$ if $i = 0$, and for $0 \leqslant j \leqslant 2$ if $i = 1$.

We view the integral as

$$\int\int_{(x,v)\in\mathscr{P}} x^i v^j \,\mathrm{d}A, \tag{43}$$

where $\mathscr{P}$ is the convex polygon in (x,v) defined by the conditions $\{x \in \mathscr{S}, v \in [q_-(x), q_+(x)], x + v\Delta t \in \mathscr{T},\}$; see Fig. 4. Using the divergence theorem we get

$$\begin{aligned} &\int\int_{(x,v)\in\mathscr{P}} x^i v^j \,\mathrm{d}A = \int_{\partial\mathscr{P}} (0, \frac{x^i v^{j+1}}{j+1}) \cdot \hat{n}\,\mathrm{d}S = \sum\nolimits_{k=0}^{n-1} \int_0^1 (x_k + \Delta t \delta x_k)^i (v_k + \Delta t \delta v_k)^{j+1} \frac{-\delta x_k}{j+1}\,\mathrm{d}t, \\ &\delta x_k = x_{(k+1)\bmod n} - x_k, \quad \delta v_k = v_{(k+1)\bmod n} - v_k. \end{aligned} \tag{44}$$

3.3. A single time step

Given cell averages $\mathbf{U}_i^n$, we summarize the steps required to obtain $\mathbf{U}_i^{n+1}$.

(1) Compute (preliminary) primitive variables $\mathbf{V}_i$ in cells $\mathscr{I}_i$.
(2) Compute (preliminary) slopes $D\mathbf{V}_i$ (e.g., using non-oscillatory interpolation).
(3) Compute Δt using (30).
(4) Limit slopes to ensure positivity of f and g using (24), (25)
(5) Adjust for conservation using (22) and (23) to get (final) primitive reconstruction $\mathbf{V}_i, D\mathbf{V}_i$.
(6) Construct $f(x, v)$ and $g(x, v)$ using (15), (16).
(7) Initialize a vector of updates $\delta\mathbf{U}_i$ to zero. For each cell $\mathscr{I}_i$,
  (a) Identify J_i, the set of indices of cells with any part within Δx of cell $\mathscr{I}_i$, excluding i itself.
  (b) For each $j \in J_i$
    (i) Compute $\delta\mathbf{U}_{i\to j} = \int_{x\in\mathscr{I}_i}\int_{x+vt\in\mathscr{I}_j} \begin{pmatrix} 1 \\ v \\ \frac{v^2}{2} \end{pmatrix} f_s(x,v) + \begin{pmatrix} 0 \\ 0 \\ 1 \end{pmatrix} g_s(x,v)\,\mathrm{d}v\,\mathrm{d}x.$
    (ii) Update $\delta\mathbf{U}_j \leftarrow \delta\mathbf{U}_j + \delta\mathbf{U}_{i\to j}$.

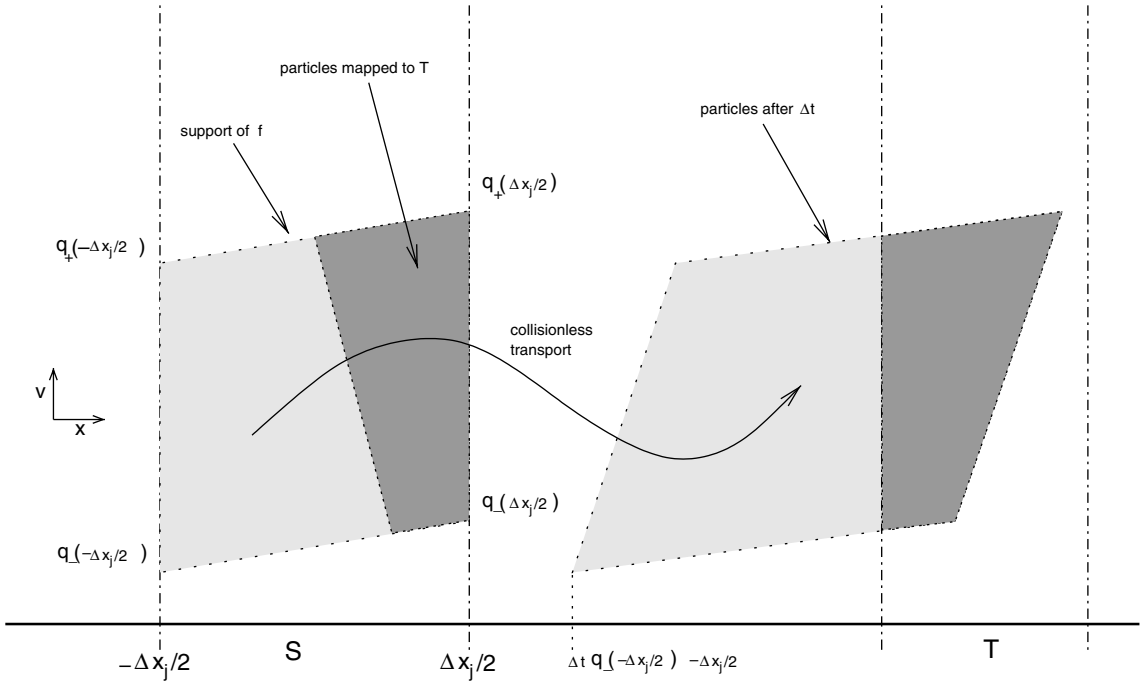

Fig. 4. Support of particles starting in source $\mathscr{S}$ and ending in target $\mathscr{T}$.

(iii) Update $\delta\mathbf{U}_i \leftarrow \delta\mathbf{U}_i - \delta\mathbf{U}_{i\to j}$.

(8) Update $\mathbf{U}_i \leftarrow \mathbf{U}_i + \delta\mathbf{U}_i/\Delta x_i$.

3.4. Boundary procedures

For one dimensional flow, reflecting boundary conditions are typically implemented by setting 'mirror image' ghost flow on the opposite side of the boundary face with identical pressure and density and opposite flow velocity normal to the boundary. This procedure can be equivalently formulated at the particle level by setting mirror image distribution functions

$$\hat{f}_0(x;v) = \begin{cases} f_0(x;v) & x > 0 \\ f_0(-x,-v) & x < 0 \end{cases}, \tag{45}$$

similarly for $g_0(x;v)$.

4. Numerical examples

In the following examples, the solution domain is $x \in [0,1]$. The grid cell boundaries are at $x_i - \frac{1}{2}$, $1 \leqslant i \leqslant N+1$ with $x_{\frac{1}{2}} = 0, x_N + \frac{1}{2} = 1$. The characteristic grid spacing is $\Delta x = \max_i \Delta x_i$. In all computations, Δt is computed according to (30), and $\gamma = 1.4$.

The piecewise linear reconstruction of the primitive variables uses a minmod limiter

$$\mathrm{D}V_i = \mathrm{minmod}(\Delta_0 V_i, 2\Delta_- V_i, 2\Delta_+ V_i)/\Delta x_i, \tag{46}$$

where $\Delta_{\pm}V_i$ are the forward/backward difference operators and $\Delta_0 V_i$ is the centered difference operator at the cell center x_i, using a 3-point parabolic interpolation. On a regular grid this reduces to the MUSCL limiter introduced in [13].

We define ς as the ratio between the largest and smallest cells,

$$\varsigma = \frac{\max_i \Delta x_i}{\min_i \Delta x_i}, \tag{47}$$

and consider four classes of grid:

- A regular grid: $\Delta x_i = \frac{1}{N}$.
- A mostly-regular grid with one small cell in the center.
- An irregular grid defined in blocks of 10, as used in ([7])

$$\Delta x_i = c_{i \bmod 10}/(5N), \tag{48}$$

where

$$c = (2, 3, 5, 10, 1, 4, 2, 3, 10, 10). \tag{49}$$

- A grid with one small cell near the left boundary at $x = 0$, with a reflecting boundary condition. This grid is relevant to Cartesian mesh cut cell grids because typically the small cells appear near solid boundaries.

For the grids with one small cell, we have used $\varsigma = 100$. The globally irregular grid has $\varsigma = 10$.

A standard test problem characterized by very strong wave interactions is the Woodward–Colella blast-wave problem introduced in [14]. The solution domain is $x \in [0, 1]$ with reflecting boundary conditions at $x = 0$ and $x = 1$. The initial condition is $\rho_0 = 1$, $u_0 = 0$, and

$$p_0(x) = \begin{cases} 1000 & 0 \leqslant x \leqslant 0.1, \\ 0.001 & 0.1 \leqslant x \leqslant 0.9, \\ 100 & 0.9 \leqslant x \leqslant 1. \end{cases} \tag{50}$$

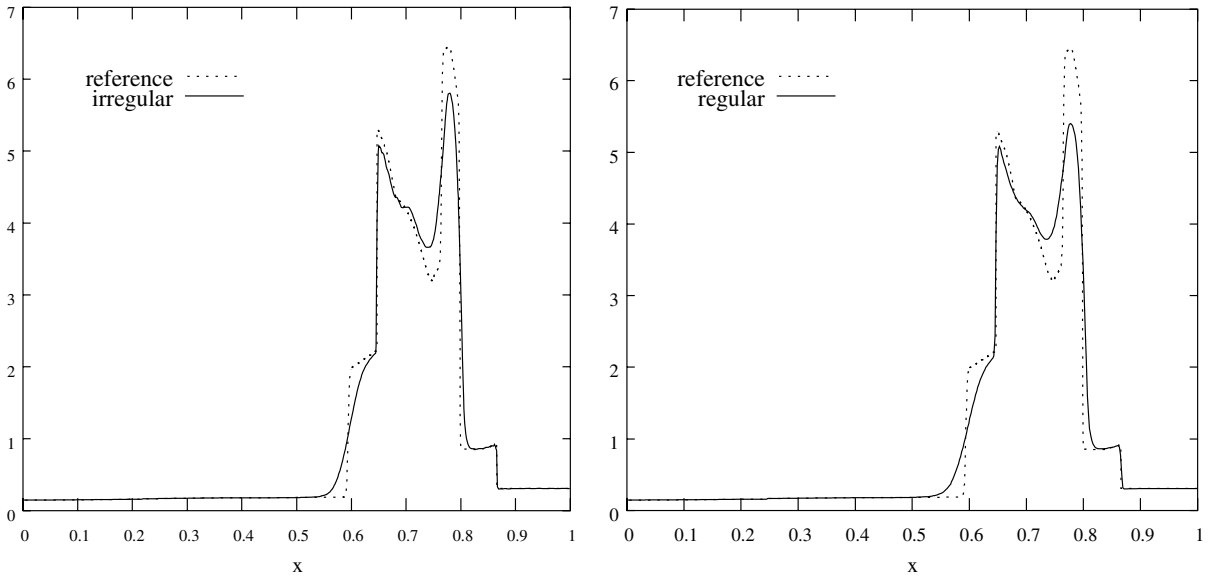

Fig. 5. Woodward–Colella double blast wave; solution density at $t = 0.038$.

We compute the solution, using minmod interpolation to $t = 0.038$ on two meshes: A regular mesh with 500 points, and an irregular mesh with 1000 points constructed according to (48) and (49). Both test meshes have the same largest cell size $\Delta x = 0.002$ and the same time step. For the irregular mesh the time step is 9 times the stable time step for a flux formulation. For comparison, we show a 10,000 cell regular grid high resolution solution. Fig. 5 shows the density of the computed solution on the regular and irregular grids as compared with the reference solution.

Another example is of a strong double expansion wave, showing the robustness of this scheme. The initial condition is again a Riemann problem

$$(\rho_L, u_l, p_l) = (1, -5, 0.4); \quad x \leqslant 0.5, \tag{51}$$

$$(\rho_R, u_r, p_r) = (1, 5, 0.4); \quad x > 0.5, \tag{52}$$

resulting in two strong expansion waves separated by a region of near vacuum. In Fig. 6 the density is shown on both a linear and log scale. Many schemes have difficulty with density and pressure positivity in such regimes (see [15]), but the kinetic scheme remains positive. The time step here is 9 times the stable time step for the flux formulation.

4.1. Smooth solutions

In the next few examples, we consider smooth flows. We turn all the slope limiters off; the results confirm that the solution converges with second order accuracy in smooth regions, on irregular grids.

4.1.1. Linear advection

The initial conditions are

$$(\rho_0(x), u_0, p_0) = (0.2\sin(2\pi x) + 2, 3, 1). \tag{53}$$

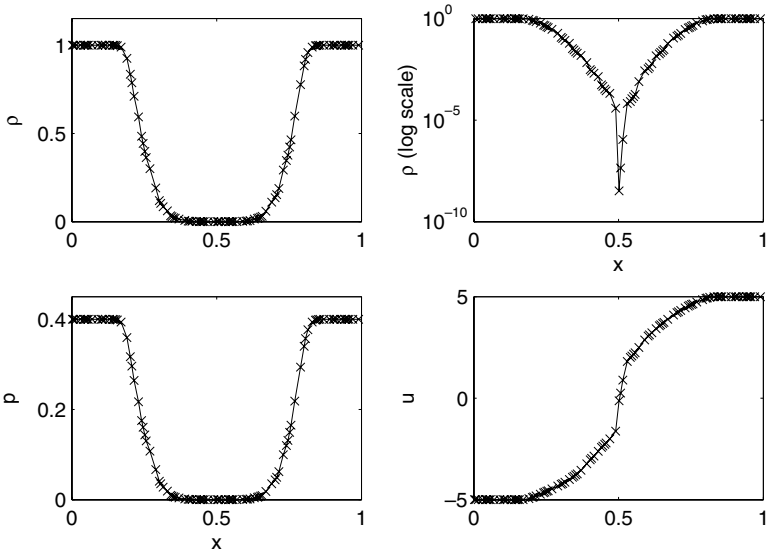

Fig. 6. Double expansion wave, solution at $t = 0.05$.

Table 1
L_1 Error in ρ for advection

N	Regular		Small		Irregular	
	$\|e\|$	$k(\Delta x)$	$\|e_{\Delta x}\|$	$k(\Delta x)$	$\|e_{\Delta x}\|$	$k(\Delta x)$
50	8.66E-5	n/a	8.55E-5	n/a	8.02E-5	n/a
100	1.55E-5	2.49	1.54E-5	2.47	1.54E-5	2.38
200	3.49E-6	2.15	3.49E-6	2.14	3.63E-6	2.09
400	8.50E-7	2.04	8.50E-7	2.04	9.21E-7	1.98
800	2.12E-7	2.00	2.12E-7	2.00	2.18E-7	2.08

corresponding to a density profile linearly transported at a speed u_0. We impose periodic boundary conditions and run the scheme until $t = 1/3$ so that the initial data has completed one period. Note that although this example describes linear transport, the scheme itself is fully non-linear.

Results are summarized in Table 1. Here, $e_{\Delta x}$ denotes the absolute error versus the exact solution, and $k(\Delta x)$ the L_1 computed order of convergence:

$$k(\Delta x) = \log_2\left(\frac{\|e_{2\Delta x}\|_1}{\|e_{\Delta x}\|_1}\right). \tag{54}$$

Convergence rates on all grids show second order behavior. In the case where there is one small cell ($\varsigma = 100$) the solution exhibits almost no change from the regular grid.

4.1.2. A rarefaction wave

As a non-linear test case, we consider the Riemann problem

$$(\rho_L, u_L, p_L) = (1.40537, 1.01655, 1.61030),$$
$$(\rho_R, u_R, p_R) = (1, 1.43322, 1).$$

producing a centered rarefaction wave whose left face propagates with velocity $-1/4$ and whose right face propagates with velocity 1/4.

As initial condition for the test case, we take the exact solution for this Riemann problem at $t = 1$. We integrate the solution to $t = 1.237$, and calculate errors over the smooth interval $[0.4, 0.6]$.

Convergence results are summarized in Table 2. On all grids, the solution converges with second order accuracy in the L_1 norm. For the small cell grid, the small cell is the location of the sonic point.

4.1.3. Weak wave reflection

In the next test case, we simulate an object embedded in the mesh, imposing reflecting boundary conditions at $x = 0$. We consider a regular grid, as well as a grid with one small cell near the solid boundary.

Table 2
L_1 Error in ρ for rarefaction wave

N	Regular		Small		Irregular	
	$\|e\|$	$k(\Delta x)$	$\|e_{\Delta x}\|$	$k(\Delta x)$	$\|e_{\Delta x}\|$	$k(\Delta x)$
50	1.04e-5	n/a	1.04e-5	n/a	1.49e-5	n/a
100	2.63e-6	1.99	2.63e-6	1.98	4.16e-6	1.84
200	6.60e-7	1.99	6.60e-7	1.99	1.38e-6	1.59
400	1.67e-7	1.98	1.69e-7	1.98	3.76e-7	1.88
800	4.24e-8	1.98	4.26e-8	1.99	1.07e-7	1.81

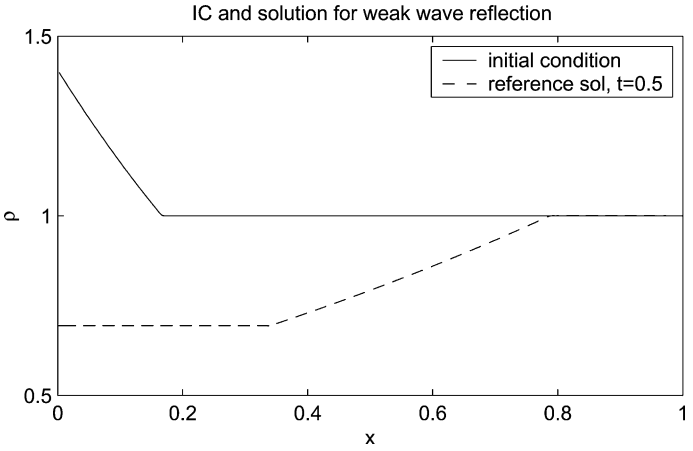

Fig. 7. Weak wave reflection test case.

Table 3
L_1 Error in ρ for rarefaction wave reflection

N	Regular		Small	
	$\|e\|$	$k(\Delta x)$	$\|e_{\Delta x}\|$	$k(\Delta x)$
50	7.46e-5	n/a	5.31e-5	n/a
100	1.71e-5	2.12	1.32e-5	2.00
200	4.12e-5	2.05	3.49e-6	1.92
400	9.95e-7	2.05	8.97e-7	1.97
800	2.36e-7	2.08	2.23e-7	2.00

The initial condition in the tests is the solution of the Riemann problem from the previous case, Galilean shifted so that the gas velocity on the left state is zero:

$$(\rho_L, u_L, p_L) = (1.40537, 0, 1.61030),$$
$$(\rho_R, u_R, p_R) = (1, 0.41667, 1).$$

The initial spread of the fan to be 1/6, and the origin of the Riemann problem is at $\frac{\sqrt{\gamma}-1/12}{3}$ so the leftmost edge of the wave starts at the reflecting boundary.

For these tests, the error is with respect to a reference solution computed on a highly refined regular grid, with $N = 3200$. The solution is computed at $t = 1/6$ and errors are calculated over the smooth interval $[0, 0.2]$. A plot of the density of the initial condition and reference solution is in Fig. 7.

Convergence tests are summarized in Table 3. Both grids converge with second order accuracy; the grid with one small cell near the boundary has slightly smaller error than the regular grid.

4.2. Discontinuous solutions

In the following tests, we turn the limiters back on and consider solutions containing shock waves.

4.2.1. A shock on an irregular grid

This test case is a leftward moving shock; the domain and grids are the same as in Section 4.1.2. The initial data is

$$(\rho_L, u_L, p_L) = (1, 0, 1), \quad x < 0.7,$$
$$(\rho_R, u_R, p_R) = (2.18182, -1.08333, 3.16667), \quad x > 0.7.$$

corresponding to a left moving shock wave with speed $s = -2$. The solution is computed at $t = 0.2$; we compare the post shock state on $[0.4, 0.6]$ with the exact answer.

Convergence results are plotted in Fig. 8. The solution behavior appears similar on all grids. The L_1 error decreases as $O(\Delta x)$, as expected for a solution with a discontinuity.

4.2.2. Shock reflection

The final test case is of a shock bouncing off a wall. We use the same shock data as in Section 4.2.1, located at $x = 0.2$. After reflection, the state on the wall is

$$(\rho_{L'}, u_{L'}, p_{L'}) = (4.267378, 0, 8.406056).$$

We solve to $t = 0.3647$, placing the reflected shock at $x = 0.3$, and compute the error over $[0, 0.2]$ to study convergence near the boundary. Table 4 shows the results.

Fig. 9 shows the computed solution on a regular grid with $N = 100$ and a grid with one small cell near the boundary. Solutions on both grids exhibit similar behaviour. The phenomenon of "wall heating", often seen with finite volume schemes, can be observed near the left hand boundary. It is interesting to note that the solution on the grid with one small cell near the boundary exhibits less heating (smaller undershoot) than the solution on the regular grid.

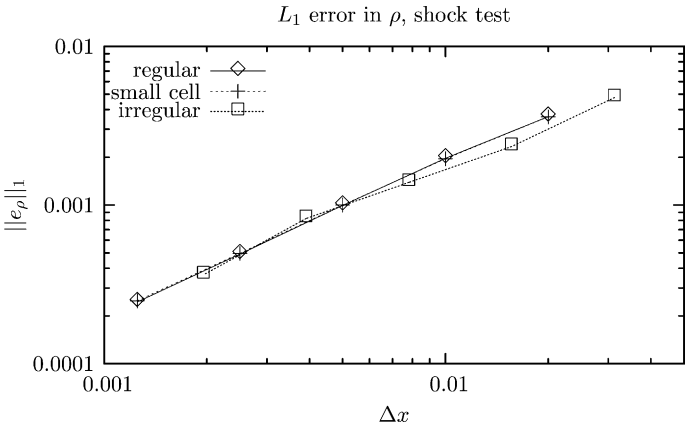

Fig. 8. Shock wave convergence test.

Table 4
L_1 Error in ρ for shock reflection

N	Regular		Small	
	$\|e\|$	$k(\Delta x)$	$\|e_{\Delta x}\|$	$k(\Delta x)$
50	7.09e-3	n/a	6.92e-3	n/a
100	3.42e-3	1.05	3.40e-3	1.03
200	1.79e-3	0.94	1.62e-3	1.07
400	9.17e-4	0.96	8.06e-4	1.01
800	4.72e-4	0.96	4.01e-4	1.01

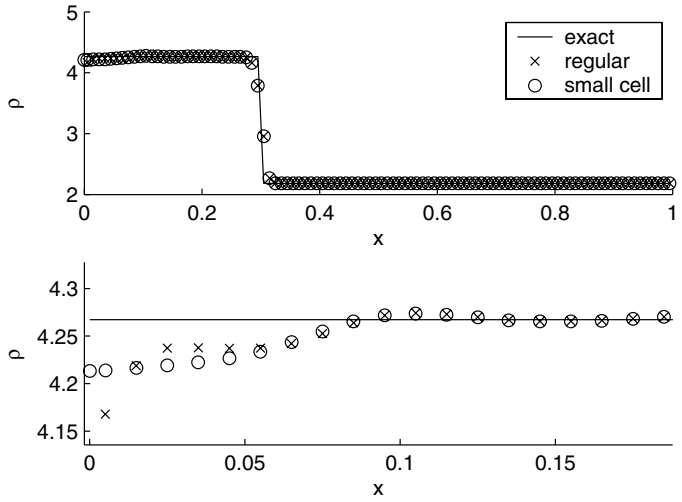

Fig. 9. Shock reflection with regular grid up to the boundary.

5. 2D Extension

In two space dimensions the Euler equations are:

$$\begin{pmatrix} \rho \\ \rho u_1 \\ \rho u_2 \\ E \end{pmatrix}_t + \begin{pmatrix} \rho u_1 \\ \rho u_1^2 + p \\ \rho u_1 u_2 \\ u_1(E+p) \end{pmatrix}_{x_1} + \begin{pmatrix} \rho u_2 \\ \rho u_1 u_2 \\ \rho u_2^2 + p \\ u_2(E+p) \end{pmatrix}_{x_2} = 0. \tag{55}$$

We denote by

$$\begin{aligned} \mathbf{U} &= (\rho, \rho u_1, \rho u_2, E)^{\mathrm{T}} \\ \mathbf{F}_1 &= \left(\rho u_1, \rho u_1^2 + p, \rho u_1 u_2, (E+p)u_1\right)^{\mathrm{T}} \\ \mathbf{F}_2 &= \left(\rho u_2, \rho u_1 u_2, \rho u_2^2 + p, (E+p)u_2\right)^{\mathrm{T}} \end{aligned} \tag{56}$$

the vectors of conserved variables and flux functions, respectively, with $u^2 = u_1^2 + u_2^2$. In general boldface denotes vector values in the spatial coordinates, i.e., $\mathbf{x} = (x_1,x_2)$, $\mathbf{v} = (v_1,v_2)$ and $\mathbf{i} = (i,j)$.

5.1. Kinetic construction

The construction of the 2D scheme follows closely the 1D construction; the pseudo-Maxwellian distributions are constructed in two space dimensions, the distributions are evolved collisionlessly, and the fluid variables are recovered by taking appropriate moments.

Particle distributions for a first order scheme in 2D were proposed in [9]. For second order accuracy, we adopt the same strategy as in the 1D case, and seek modified distributions of the form

$$f_{2s}(\mathbf{x};\mathbf{v}) = \frac{\rho}{T}\chi(w_1)\chi(w_2)(1 + a_1(w_1^2 - 1) + a_2(w_2^2 - 1) + a_3 w_1 w_2), \tag{57}$$

$$g_{2s}(\mathbf{x};\mathbf{v}) = \rho\beta\chi(w_1)\chi(w_2)(1 + b_1 w_1 + b_2 w_2). \tag{58}$$

Here $w_k = \frac{v_k - u_k(\mathbf{x})}{\sqrt{T(\mathbf{x})}}$. With the choices

$$a_1 = \frac{5}{8}\Delta t((3-\gamma)\mathsf{D}_1 u_1 + (1-\gamma)\mathsf{D}_2 u_2), \tag{59}$$

$$a_2 = \frac{5}{8}\Delta t((1-\gamma)\mathsf{D}_1 u_1 + (3-\gamma)\mathsf{D}_2 u_2), \tag{60}$$

$$a_3 = \frac{\Delta t}{2}(\mathsf{D}_2 u_1 + \mathsf{D}_1 u_2), \tag{61}$$

$$b_1 = \Delta t\left(1 + \frac{4(\gamma-1)}{5(2-\gamma)}\right)\mathsf{D}_1\sqrt{T} - \frac{3(\gamma-1)}{10(2-\gamma)}\sqrt{T}\frac{\mathsf{D}_1\rho}{\rho}, \tag{62}$$

$$b_2 = \Delta t\left(1 + \frac{4(\gamma-1)}{5(2-\gamma)}\right)\mathsf{D}_2\sqrt{T} - \frac{3(\gamma-1)}{10(2-\gamma)}\sqrt{T}\frac{\mathsf{D}_2\rho}{\rho}, \tag{63}$$

where

$$\beta = \frac{2-\gamma}{\gamma-1} - \frac{2}{5}(a_1 + a_2) \tag{64}$$

an elementary calculation verifies that

$$\begin{aligned}\widetilde{\mathbf{U}}(\mathbf{x},\Delta t) &= \int\int_{\mathbb{R}^2} \begin{pmatrix} 1 \\ v_1 \\ v_2 \\ v^2/2 \end{pmatrix} f_{2s}(\mathbf{x},\Delta t;\mathbf{v}) + \begin{pmatrix} 0 \\ 0 \\ 0 \\ 1 \end{pmatrix} g_{2s}(\mathbf{x},\Delta t;\mathbf{v})\,\mathrm{d}\mathbf{v} \\ &= \int\int_{\mathbb{R}^2} \begin{pmatrix} 1 \\ v_1 \\ v_2 \\ v^2/2 \end{pmatrix} f_{2s}(\mathbf{x}-\Delta t\ \mathbf{v};\mathbf{v}) + \begin{pmatrix} 0 \\ 0 \\ 0 \\ 1 \end{pmatrix} g_{2s}(\mathbf{x}-\Delta t\ \mathbf{v};\mathbf{v})\,\mathrm{d}\mathbf{v} = \mathbf{U}(\mathbf{x},\Delta t) + \mathrm{O}(\Delta t^3).\end{aligned} \tag{65}$$

L_1 stability and positivity of ρ and T carry through as in the 1D case provided the microscopic reconstruction is positive; see [9] and [16]. To that end, we limit the parameters a_1, a_2, a_3, b_1 and b_2 as follows:

$$|a_1| \leqslant \frac{1}{6}, \quad |a_2| \leqslant \frac{1}{6}, \quad |a_3| \leqslant \frac{1}{9}, \tag{66}$$

$$|b_1| \leqslant (2\sqrt{3})^{-1}, \quad |b_2| \leqslant (2\sqrt{3})^{-1}, \tag{67}$$

5.2. Interpolation

In each grid cell $\mathscr{I}_\mathbf{i}$ we interpolate the primitive variables $\mathbf{V} = (\rho, u_1, u_2, r)$

$$\begin{aligned}\mathbf{V}_\mathbf{i}(\mathbf{x}) &= (\rho_\mathbf{i}(\mathbf{x}), u_{1\mathbf{i}}(\mathbf{x}), u_{2\mathbf{i}}(\mathbf{x}), r_i(\mathbf{x}))^{\mathrm{T}} \\ &= (\rho_\mathbf{i}, u_{1\mathbf{i}}, u_{2\mathbf{i}}, r_\mathbf{i}) + (\mathsf{D}_1\rho_\mathbf{i}, \mathsf{D}_1 u_{1\mathbf{i}}, \mathsf{D}_1 u_{2\mathbf{i}}, \mathsf{D}_1 r_\mathbf{i})(x_1 - x_{1,\mathbf{i}}) + (\mathsf{D}_2\rho_\mathbf{i}, \mathsf{D}_2 u_{1\mathbf{i}}, \mathsf{D}_2 u_{2\mathbf{i}}, \mathsf{D}_2 r_\mathbf{i})(x_2 - x_{2,\mathbf{i}}).\end{aligned} \tag{68}$$

Away from the boundary, we apply non-oscillatory interpolation in each coordinate direction using the limiter (46).

For cells that are near the boundary, the centroids will not in general line up in coordinate directions. For the slopes in a cell (i, j) we use one-sided differencing by fitting a linear function in $\mathbf{x}$ through the data in that cell and that in cell $(i \pm 1, j \pm 1)$, see Fig. 10. Each three point stencil is used to compute slopes normal and tangential to the boundary segment, and the normal and tangential slope with minimum absolute value among these candidates is used.

The scheme allows considerable freedom in constructing the interpolation provided the requirements for a positive reconstruction are met. For the test cases with smooth data where no limiting is required we fit a function of the form $q + \mathsf{D}_{\hat{t}} q\hat{t} + \mathsf{D}_{\hat{t}}^2 q\hat{t}^2 + \mathsf{D}_{\hat{n}} q\hat{n}$, where $(\hat{t}, \hat{n})$ are the normal and tangential coordinates of the boundary cell. For better accuracy in the tangential direction, we use the four point stencil consisting of the main cell, its two neighbors near the boundary, and a neighbor out in the normal direction.

Conservation adjustment ensures that the piecewise linear reconstruction (68) is conservative. In each cell $\mathscr{S} = \mathscr{I}_{\mathbf{i}}$, we adjust (ρ, u_1, u_2, r) so that

$$\begin{aligned}
\int\int_{\mathscr{S}} \hat{\rho}\,\mathrm{d}\mathbf{x} &= \int\int_{\mathscr{S}} \rho(\mathbf{x})\,\mathrm{d}\mathbf{x},\\
\int\int_{\mathscr{S}} \rho\hat{u}_k\,\mathrm{d}\mathbf{x} &= \int\int_{\mathscr{S}} \rho(\mathbf{x})u_k(\mathbf{x})\,\mathrm{d}\mathbf{x},\\
\int\int_{\mathscr{S}} \hat{E}\,\mathrm{d}\mathbf{x} &= \int\int_{\mathscr{S}} \rho(\mathbf{x})\left(\frac{r(\mathbf{x})^2}{\gamma-1} + \frac{1}{2}\left(u_1(\mathbf{x})^2 + (u_2(\mathbf{x})^2\right)\right)\mathrm{d}\mathbf{x}.
\end{aligned} \tag{69}$$

These constraints can easily be satisfied using a procedure similar to that in Section 2.4; detailed formulae are in [16]. The adjusted interpolant of r remains positive over the grid cell provided

$$|\mathsf{D}_k u_j| \leqslant \frac{\sqrt{(\gamma-1)T_{\mathbf{i}}}}{2\Delta x} \tag{70}$$

for $k, j = 1, 2$ and

$$|\mathsf{D}_k r| \leqslant \frac{\sqrt{T_{\mathbf{i}}}}{2\sqrt{3}\Delta x}. \tag{71}$$

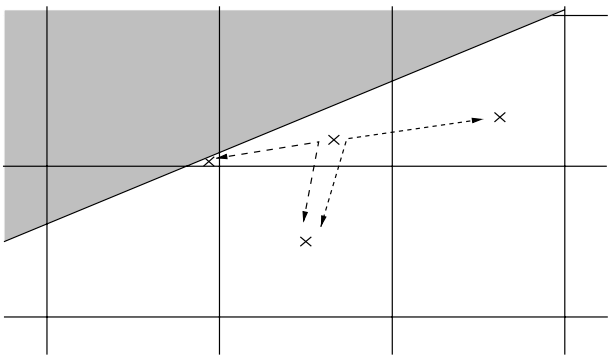

Fig. 10. Interpolation stencils near a boundary.

In practice this limiter is nearly always redundant with the limitations inherent in the non-oscillatory interpolation.

5.3. Evaluating 2D transport

In analogy with the 1D case, we set the time step as

$$\Delta t \leqslant \frac{\Delta x}{\sqrt{2}\max_{\mathbf{i}}\{\max_k |u_{k,\mathbf{i}}| + \sqrt{3T_{\mathbf{i}}}\}}. \tag{72}$$

where Δx is a parameter typically chosen to coincide with the regular grid mesh spacing. With the choice (72) no particle in the initial distributions $f_{2s}(\mathbf{x};\mathbf{v})$ and $g_{2s}(\mathbf{x};\mathbf{v})$ will travel more than Δx over the time interval Δt.

The transport of conserved quantities between two cells is given by

$$\int\int_{\mathscr{S}}\int\int_{\mathbf{x}+\mathbf{v}\Delta t\in\mathscr{T}} \begin{pmatrix} 1 \\ v_1 \\ v_2 \\ \frac{v^2}{2} \end{pmatrix} f_{\mathbf{i}}(\mathbf{x};\mathbf{v}) + \begin{pmatrix} 0 \\ 0 \\ 0 \\ 1 \end{pmatrix} g_{\mathbf{i}}(\mathbf{x};\mathbf{v})\,\mathrm{d}\mathbf{v}\,\mathrm{d}\mathbf{x}. \tag{73}$$

Taylor expansion as in Section 3.1 and Section 3.2 leads to evaluation of integrands of the form

$$\int\int_{\mathscr{S}}\int\int_{\mathbf{x}+\mathbf{v}\Delta t\in\mathscr{T}\,\mathbf{w}\in[-\sqrt{3},\sqrt{3}]^2} x_1^m x_2^n v_1^k v_2^l\,\mathrm{d}\mathbf{v}\,\mathrm{d}\mathbf{x}, \tag{74}$$

for

$$\begin{cases} m=0, & n=0, & k+l\leqslant 4, \\ m=1, & n=0, & k+l\leqslant 2, \\ m=0, & n=1, & k+l\leqslant 2, \end{cases} \tag{75}$$

where $\mathscr{S}$ and $\mathscr{T}$ are polygons. We note that only the five moments $m = 0$, $n = 0$, $k + l \leqslant 2$ need be accurate to $O(\Delta x^2)$; the rest may be accurate only to $O(\Delta x)$.

The domain of integration for (74) is in general a convex polytope in $\mathbb{R}^4$. A technique for evaluating integrals over such domains can be found in [17]. Details on how to take advantage of the special structure of

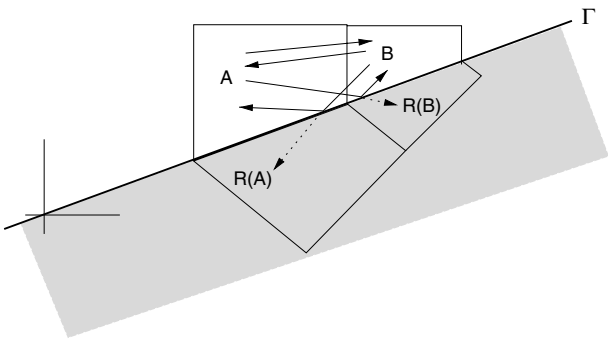

Fig. 11. 2D particle reflection.

the domain of integration to make this operation efficient, as well as discussion of how to implement (74) in the general case can be found in [16].

5.4. 2D Boundary procedures

Reflecting boundary condition in 2D are implemented by creating reflected cells across the domain boundary and initializing them from fluid data with reflected normal velocity (see Fig. 11).

6. 2D Numerical examples

6.1. Rectangular grid

The first example is of a 2D periodic oblique flow over the unit square $\mathbf{x} \in [0,1]^2$. We consider two grids: (i) a regular grid; (ii) a rectangular grid with a small narrow strip of cells in each of the coordinate directions, crossing in the center of the domain. This grid contains one small cell and two strips of elongated rectangular cells. The small cell size is $(0.173)^2$ or $(0.01)^2$ of the regular cell.

The initial condition is

$$(\rho_0(\mathbf{x}), u_1, u_2, p_0) = (0.3\sin(2\pi x_1)\sin(2\pi x_2) + 2,\ -2,\ 2,\ 1), \tag{76}$$

with periodic boundary conditions; we run the scheme until the density profile has moved one period. The numerical results are summarized in Table 5 where k is the order of convergence:

$$k(\Delta x) = \log_2\left(\frac{\|e_{2\Delta x}\|}{\|e_{\Delta x}\|}\right). \tag{77}$$

On both the regular and irregular grids the scheme converges with second order accuracy with virtually no difference in absolute error.

6.2. Oblique channel shock tube

We consider one-dimensional flow in an oblique channel, and study convergence of solutions in the presence of a rigid boundary and cut cells as they appear in Cartesian mesh grids. Fig. 12 shows a schematic of this embedded boundary mesh. To examine convergence near the boundary, we compute the L_1 norm over the cut cells and all of their neighbors. These are precisely the grid cells that interact directly with the boundary over a single time step.

Table 5
L_1 errors in ρ for 2D advection

Δx	$\|e_{\text{reg}}\|$	k(reg)	$\|\|e_{\varsigma^{-1}=0.01}\|\|$	$k(\varsigma^{-1}=0.01)$	$\|\|e_{\varsigma^{-1}=0.173}\|\|$	$k(\varsigma^{-1}=0.173)$
2^{-4}	5.42e-3		5.21e-3		5.11e-3	
2^{-5}	8.00e-4	2.76	7.91e-4	2.72	7.84e-4	2.70
2^{-6}	1.20e-4	2.74	1.29e-4	2.62	1.28e-4	2.61
2^{-7}	2.45e-5	2.29	2.46e-5	2.39	2.46e-5	2.38
2^{-8}	5.45e-6	2.17	5.46e-6	2.18	5.45e-6	2.17
2^{-9}	1.29e-6	2.08	1.29e-6	2.08	1.29e-6	2.08
2^{-10}	3.16e-7	2.03	3.16e-7	2.03	3.16e-7	2.03

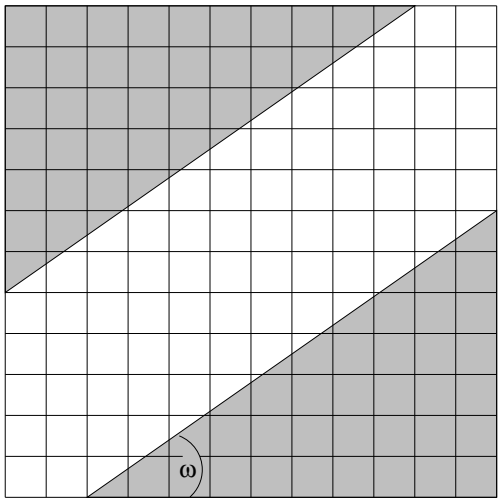

Fig. 12. Schematic of angled channel test mesh, angle ω.

Initial conditions are given by the shock tube data along the channel

$$\mathbf{V}_L = (\rho, u_1, u_2, p)_L = (1, 0, 0, 1)$$
$$\mathbf{V}_R = (\rho, u_1, u_2, p)_R = (0.125, 0, 0, 0.1).$$

The domain $[0,1]^2$ is discretized by an underlying 100×100 mesh. The angle of the channel is $\omega = \pi/6$. Density contours of the computed solution at $t = 0.15$ are shown in Fig. 13. Fig. 14 shows a slice of the computed density along the middle of the channel and the upper boundary. The agreement between the solution along boundary and the solution in the interior is excellent.

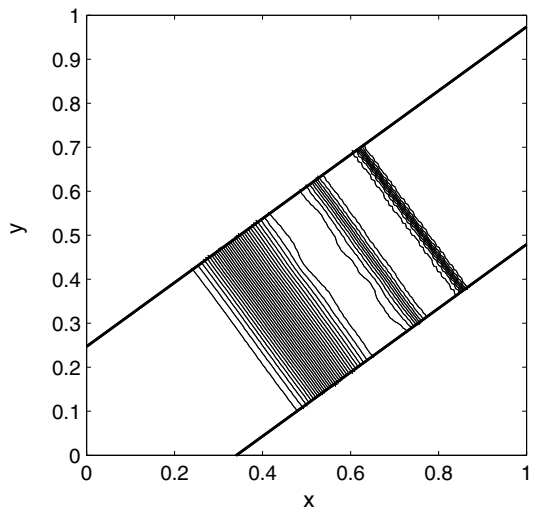

Fig. 13. Channel shock tube: contour plot of ρ.

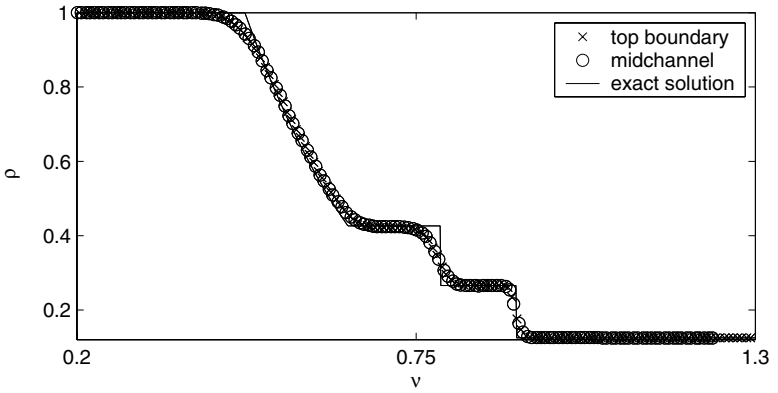

Fig. 14. Channel shock tube: ρ upper boundary and interior slices.

6.3. Shock wave

In this test, the initial data correspond to a planar shock wave moving with a speed of 2 along a $\omega = \pi/5$ channel.

$$(\rho, u_1, u_2, p)_R = (1, 0, 0, 1)$$
$$(\rho, u_1, u_2, p)_L = (24/11, 13\cos(\omega)/12, 13\sin(\omega)/12, 19/6).$$

We compute the solution at $t = 0.2$ and examine L_1 convergence in the whole domain and along the embedded boundary. Table 6 summarizes the results for ρ; other components behave similarly. The scheme exhibits the expected first order convergence on the grid as a whole as well as near to first order convergence in the narrow strip of cells near the boundary; $L_{1,\partial}$ denotes the norm in the cells adjacent to the boundary and their neighbors.

6.4. Advection

To examine convergence of the scheme on smooth solutions in the presence of the embedded boundary we again study the advection of a density wave aligned with the channel. The problem is similar to the one in [4]. The initial conditions are:

$$(\rho_0(\mathbf{x}), u_1, u_2, p_0) = (2 + h(\mathbf{x}), \cos(\omega), \sin(\omega), 1), \tag{78}$$

where

$$h(\mathbf{x}) = \begin{cases} 10\exp\left(-((1.5 - 5v)(2.5 - 5v))^{-1}\right), & 0.3 < v < 0.5, \\ 0, & \text{otherwise.} \end{cases} \tag{79}$$

Table 6
L_1 errors for a shock in an oblique channel

Δx	$\|e\|_1$	$k(L_1)$	$\|e\|_{1,\partial}$	$k(L_{1,\partial})$
2^{-6}	6.26e-3		1.11e-3	
2^{-7}	3.08e-3	1.02	2.57e-4	1.11
2^{-8}	1.57e-3	0.98	7.47e-5	0.78
2^{-9}	7.83e-4	1.00	2.18e-5	0.77

Table 7
L_1 and L_∞ errors of ρ for linear transport in channel

Δx	$\|e\|_1$	$k(L_1)$	$\|e\|_{1,\partial}$	$k(L_{1,\partial})$	$\|e\|_\infty$	$k(L_\infty)$
2^{-6}	5.28e-3		8.62e-5		1.15e-2	
2^{-7}	1.10e-4	2.26	9.24e-6	2.22	3.23e-3	1.83
2^{-8}	2.2e-5	2.32	9.26e-7	2.32	7.63e-4	2.08
2^{-9}	4.55e-6	2.27	1.05e-7	2.14	2.05e-4	1.90

where v is the coordinate aligned with the channel. For this calculation we turn all limiters off, and compute the solution at $t = 0.2$, comparing with the exact solution. The solution converges with second order accuracy in L_1 as well as L_∞ over the entire domain as well as in the boundary cells in all variables; see Table 7. We note that the cell volumes in this problem span many orders of magnitude: on the coarsest grid the volume ratio of smallest to regular grid cells is 4.4×10^{-4} and on the finest grid it is 2.7×10^{-6}.

These results compare very well with other methods [7,1,4].

6.5. Oblique shock reflection

Finally, we have computed the reflection of a shock on an $\omega = \pi/6$ ramp. Initial data is

$$(\rho_R, u_{1R}, u_{2R}, p_R) = (1, 0, 0, 1), \quad x > 0.1,$$
$$(\rho_L, u_{1L}, u_{2L}, p_L) = (3.7336083, 2.48629952, 0, 9.44305), \quad x < 0.1,$$

producing a shock wave moving to the right with Mach number $M = 2.87$. The ramp has reflecting boundary conditions. Fig. 15 shows density contours on an underlying 200×200 Cartesian mesh at $t = 0.22$. Flow features are cleanly resolved and do not appear to exhibit any oscillations or artifacts due to the embedded boundary. The Mach stem is perpendicular to the ramp, and the slip surface is cleanly captured. On this mesh, the smallest grid cell is 2.3×10^{-5} the size of a regular grid cell.

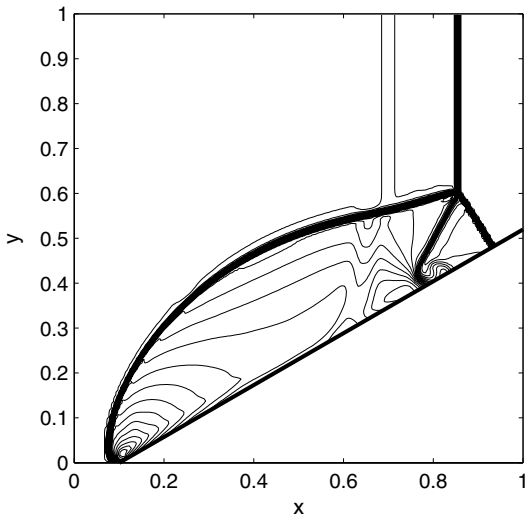

Fig. 15. Mach 2.78 shock on 30° ramp: density contours.

7. Conclusions

We have presented an implementation of a kinetic scheme for gas dynamics on arbitrary grids that does not suffer from the small-cell problem typical of Cartesian meshes. It is unconditionally stable and practical to implement for a time step constrained by regular mesh spacing. The scheme is L_1 stable and positive in density and internal energy. It converges with second order accuracy on irregular grids.

References

[1] W.J. Coirier, K.G. Powell, An assessment of Cartesian-mesh approaches for the Euler equations, Journal of Computational Physics 117 (1995) 121–131.
[2] J.J. Quirk, An alternative to unstructured grids for computing gas dynamic flows around arbitrarily complex two-dimensional bodies, Computers and Fluids 23 (1) (1994) 125–142.
[3] R.B. Pember, J.B. Bell, P. Colella, W.Y. Crutchfield, M.L. Welcome, An adaptive Cartesian grid method for unsteady compressible flow in irregular regions, Journal of Computational Physics 120 (1995) 278–304.
[4] D. Modiano and P. Colella, A Higher-order embedded boundary meothod for time-dependent simulation of hyperbolic conservation laws, Tech. Rep. LBNL-45239, Lawrence Berkeley National Laboratory, Berkeley, CA 94720, March 2000.
[5] D. Calhoun, R.J. LeVeque, A Cartesian grid finite-volume method for the advection diffusion equation in irregular geometries, Journal of Computational Physics 157 (2000) 143–180.
[6] R.J. LeVeque, A large time step generalization of Godunov's method for systems of conservation laws, SIAM Journal of Numerical Analysis 22 (1985) 1051–1073.
[7] M.J. Berger, C. Helzel, R.J. LeVeque, H-box methods for the approximation of hyperbolic conservation laws on irregular grids, SIAM Journal of Numerical Analysis 41 (3) (2003) 893–918.
[8] H. Forrer, R. Jeltsch, A higher-order boundary treatment for cartesian-grid methods, Journal of Computational Physics 140 (1998) 259–277.
[9] B. Perthame, Second order Boltzmann schemes for compressible Euler equations in one and two space dimensions, SIAM Journal of Numerical Analysis 29 (1) (1992) 1–19.
[10] H. Öksüzoğlu. State vector splitting: A numerical scheme for the Euler equations. Ph.D. Thesis, Stanford University, 1992.
[11] S. Chapman, T.G. Cowling, The Mathematical Theory of Non-Uniform Gases, third ed., Cambridge Mathematical Library, Cambridge University Press, Cambridge, 1970.
[12] B. Perthame, Boltzmann type schemes for gas dynamics and the entropy property, SIAM Journal of Numerical Analysis 27 (1990) 1405–1421.
[13] B. van Leer, Toward the ultimate conservative difference scheme V: A second order sequel of Godunov's Method, Journal of Computational Physics 32 (1979) 101–136.
[14] P. Woodward, P. Colella, The numerical solution of two-dimensional fluid flow with strong shocks, Journal of Computational Physics 54 (1984) 115–173.
[15] B. Einfeldt, C.D. Munz, P.L. Roe, B. Sjögreen, On Godunov-type methods near low densities, Journal of Computational Physics 92 (2) (1991) 273–295.
[16] B. Keen, A Kinetic Scheme for Gas Dynamics on Arbitrary Grids, Ph.D. Thesis, University of Michigan, 2004..
[17] J.B. Lasserre, Integration on a convex polytope, Proceedings of the American Mathematical Society 126 (6) (1998) 2433–2441.